Optics Letters

Giant optical second- and third-order nonlinearities at a telecom wavelength

CHING-FU CHEN,[1,†] FANGLIN TIAN,[1,†] JUNXIAO ZHOU,[1,†] JACKSON C. WAGNER,[2] WEI XIONG,[1,2,3] AND ZHAOWEI LIU[1,3,4,*]

[1] *Department of Electrical and Computer Engineering, University of California, San Diego, 9500 Gilman Drive, La Jolla, California 92093, USA*
[2] *Department of Chemistry and Biochemistry, University of California, San Diego, 9500 Gilman Drive, La Jolla, California 92093, USA*
[3] *Materials Science and Engineering Program, University of California, San Diego, 9500 Gilman Drive, La Jolla, California 92093, USA*
[4] *Center for Memory and Recording Research, University of California, San Diego, 9500 Gilman Drive, La Jolla, California 92093, USA*
[†] *These authors contributed equally to this work.*
[*] *zhaowei@ucsd.edu*

Received 25 April 2024; revised 30 May 2024; accepted 4 June 2024; posted 7 June 2024; published 25 June 2024

A material platform that excels in both optical second- and third-order nonlinearities at a telecom wavelength is theoretically and experimentally demonstrated. In this TiN-based coupled metallic quantum well structure, electronic subbands are engineered to support doubly resonant inter-subband transitions for an exceptionally high second-order nonlinearity and provide single-photon transitions for a remarkable third-order nonlinearity within the 1400–1600 nm bandwidth. The second-order susceptibility $\chi^{(2)}$ reaches 2840 pm/V at 1440 nm, while the Kerr coefficient n_2 arrives at 2.8×10^{-10} cm^2/W at 1460 nm. The achievement of simultaneous strong second- and third-order nonlinearities in one material at a telecom wavelength creates opportunities for multi-functional advanced applications in the field of nonlinear optics.

https://doi.org/10.1364/OL.528340

Nonlinear optics has emerged as a pivotal research domain following the advent of lasers in the 1960s. Optical second-order and third-order nonlinearities play crucial roles in this field, offering a rich tapestry of phenomena and applications that span a wide range of disciplines. These nonlinear effects arise from the interaction of intense light fields with materials, leading to a plethora of fascinating optical behaviors. Second-order nonlinear processes, such as second-harmonic generation (SHG) and sum-frequency generation (SFG), enable frequency conversion and coherent light generation, laying the foundation for breakthroughs in telecommunications [1], bioimaging [2], and quantum information processing [3]. Meanwhile, third-order nonlinearities, including processes such as four-wave mixing and Kerr effect, give rise to phenomena such as nonlinear optical wave mixing and self-phase modulation. These effects are harnessed for applications such as supercontinuum generation [4], frequency comb generation [5,6], ultrafast optical switching [7–9], and tunable functional meta-devices [10,11].

The key to realize numerous useful applications is the material's optical nonlinearity, which is commonly weak for both second- and third-order nonlinearities in naturally existing materials. Moreover, the second-order nonlinearity is rare because it essentially only exists in centrosymmetry-broken materials. For typical materials with high second-order nonlinearity, such as $LiNbO_3$ and transition metal dichalcogenides (TMDs), they exhibit only moderate third-order nonlinearity. Conversely, materials such as graphene and semiconductor quantum dots possess high third-order nonlinearity but not second-order nonlinearity due to their centrosymmetric structures. Thus, it is difficult to find a material with both strong second- and third-order nonlinearity in practice.

Recently, we demonstrated a strong second-order nonlinearity in coupled asymmetric TiN metallic quantum wells (QWs) [12] and single asymmetric Au metallic QW [13] at the near-infrared (NIR) wavelength of 920 and 940 nm, respectively. In different contexts, we also showed strong third-order nonlinearity in a single TiN metallic QW [14] and a single Au metallic QW [15] at the NIR wavelength of 2 and 900 nm, respectively. Yet, the strong second- and third-order nonlinearities have not been combined in one material system and at the same wavelength range.

In this work, we carefully design a pair of coupled asymmetric TiN metallic QWs to simultaneously achieve giant second- and third-order nonlinearities at a telecom wavelength. Within the bandwidth of 1400–1600 nm, the second-order susceptibility $\chi^{(2)}$ reaches 900–2840 pm/V, while the Kerr coefficient n_2 hits $1.1\text{–}2.8 \times 10^{-10}$ cm^2/W at the same time. The peak values appear at 1440 and 1460 nm, respectively. Our findings pave the way for remarkable capabilities and flexibilities in the realm of photonics and nonlinear optics. By harnessing the second- and third-order nonlinearities, this material can serve as a versatile platform for multi-functional advanced applications in telecom systems, microscopy, quantum information technologies, ultrafast laser pulse manipulation, and optical modulation, ushering in a new era of innovation and technological advancement in nonlinear optics.

Figure 1(a) illustrates the schematic of the material system possessing ultrahigh optical second- and third-order nonlinearities. It is essentially a unit of coupled metallic quantum wells (cMQWs) consisting of two asymmetric TiN metallic QWs with

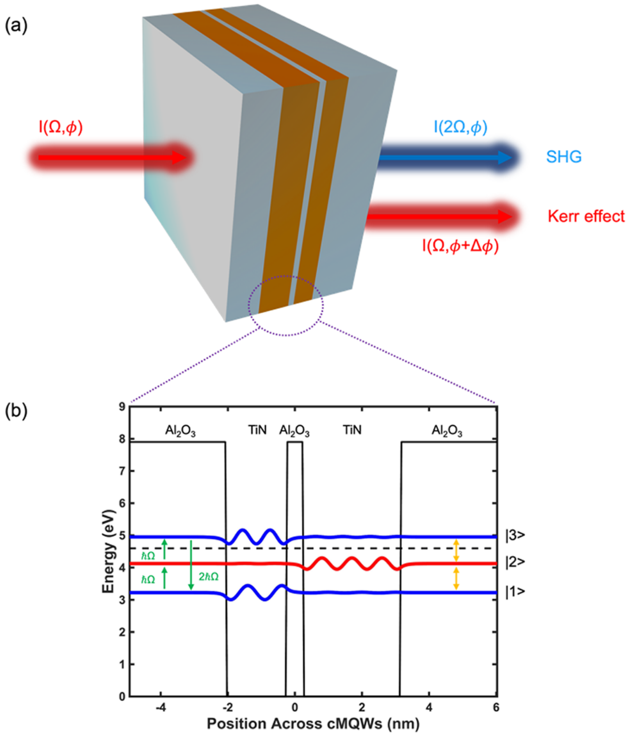

Fig. 1. (a) Schematic of the cMQW material system having both high second- and third-order nonlinearities for frequency doubling (SHG) and phase modulation (Kerr effect), respectively. (b) Conduction band diagram and the electron wavefunctions related to the enhanced nonlinear phenomena at the telecom wavelength. Thicknesses of TiN|Al_2O_3|TiN are 1.8|0.5|2.8 nm. Doubly resonant ISBTs supporting strong second-order nonlinearity are shown in green, while single-photon ISBTs providing strong third-order nonlinearity are shown in orange.

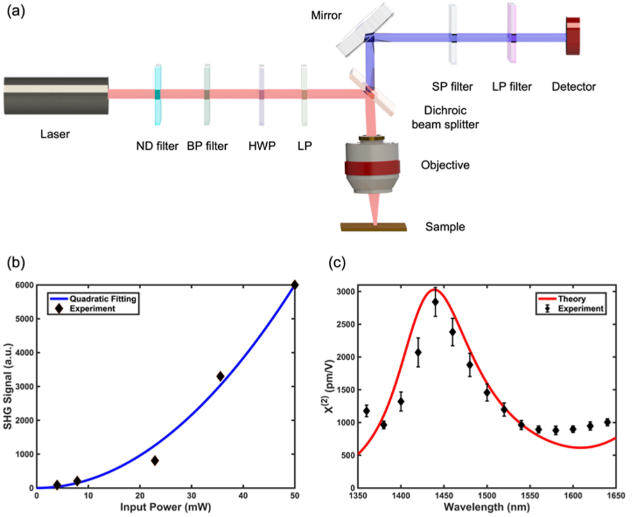

Fig. 2. (a) Optical setup of SHG measurement for $\chi^{(2)}$ characterization. (b) Power relation between the input pump power and output SHG signal. The quadratic fitting curve is exponential to the power of 2.0. (c) Spectral response of $\chi^{(2)}$ derived from the experiment in comparison with the theoretical calculation.

one Al_2O_3 dielectric barrier in between. The ultrathin TiN QWs provide inter-subband transitions (ISBTs) aligned to the photon energy of the incident light, supporting strong second- and third-order nonlinear optical processes. Figure 1(b) shows the conduction band diagram and the electron wavefunctions related to the enhanced nonlinear phenomena at the telecom wavelength. Thicknesses of TiN QWs are selected as 1.8 and 2.8 nm, respectively, while the Al_2O_3 barrier is 0.5 nm to allow strong electron tunneling. On one hand, the strong second-order nonlinearity is supported by the three equally spaced electronic subbands |1>, |2>, and |3> that form doubly resonant ISBTs, as depicted by the green arrows. Enhanced frequency doubling $\hbar\Omega + \hbar\Omega = 2\hbar\Omega$ occurs, where $\hbar\Omega = 0.86$ eV corresponds to 1440 nm in wavelength. On the other hand, the strong third-order nonlinearity, referred to as Kerr nonlinearity in this paper, is also boosted by single-photon ISBTs between |1> & |2> and |2> & |3> (orange arrows). As a result, this cMQW material is competent at both second- and third-order nonlinear optical processes in the telecom range.

The cMQ sample is prepared by reactive magnetron sputtering (AJA ATC Orion 8 RF Sputtering System), where the ultrathin films in the order of TiN|Al_2O_3|TiN|Al_2O_3 (1.8|0.5|2.8|3.0 nm) are epitaxially grown onto double-side-polished and c-plane (0001) oriented sapphire wafers. In addition to the main cMQW layers, the last Al_2O_3 acts as a barrier and protective covering layer on the top. The TiN QWs are deposited by reactively sputtering the Ti target in the chamber of Ar and N_2 mixture, while the Al_2O_3 barrier and covering are deposited by directly sputtering the Al_2O_3 target in the chamber of only Ar. The mastery of this fabrication technique for cMQWs has been consistently achieved as demonstrated in our previous work [12,14,16,17].

For the second-order nonlinear process, the three equally spaced electronic subbands form doubly resonant ISBTs and contribute to the large second-order susceptibility $\chi^{(2)}$, which is calculated based on the quantum electrostatic model [12] using the following equation:

$$\chi^{(2)}(\omega) = \frac{n_i - n_{ii}}{\hbar^2 \varepsilon_o} \frac{e^3 z_{i,ii} z_{ii,iii} z_{iii,i}}{(\omega - \Omega - i\Gamma_{ii,i})(2\omega - 2\Omega - i\Gamma_{iii,i})}, \quad (1)$$

where ω is the frequency of the incident light, Ω is the frequency of doubly resonant transition, n_i is the electron density in the ith subband, $\hbar$ is the reduced Planck constant, ε_o is the vacuum permittivity, and e is the electron charge. Here, $ez_{i,ii}$ and $\Gamma_{ii,i}$ represent the dipole moment and the decay rate at corresponding subbands. The choice of these QW thicknesses results in a $\chi^{(2)}$ peak at a doubly resonant transition frequency Ω at 1440 nm.

To characterize the large second-order nonlinearity, SHG measurement is conducted using the optical setup depicted in Fig. 2(a). The laser pulse used in this work is produced by a Yb-based femtosecond laser (Light Conversion, Carbide) pumping into an optical parametric amplifier (OPA, Light Conversion, Orpheus-HP). The pulse duration is 250 fs, while the repetition rate is 25 kHz. The wavelength is scanned from 1360 to 1640 nm for the fundamental light in the SHG measurement. On the excitation end, a neutral density filter (ND filter) is used to tune the input light power. Peak intensities at different wavelengths are controlled within few GW/cm^2 for accurate $\chi^{(2)}$ spectral response characterization. A bandpass filter (BP filter) ensures a clean excitation spectrum, whereas a half-wave plate (HWP) and a linear polarizer (LP) enable a p-polarization incidence, creating an electric field component in the out-of-plane direction of the sample during oblique incidence to effectively excite the doubly resonant ISBTs in our cMQW system for a strong second-order nonlinear process. A reflective Schwarzschild objective (PIKE Technologies, 20×, 0.7 NA) is used to excite and collect second-harmonic (SH) signals at 45° angle at the same time. On the receiving end, a short-pass filter (SP filter) and a long-pass filter (LP filter) are used to block light at fundamental and third-harmonic wavelengths, respectively. A photomultiplier tube (PMT, Hamamatsu, H10721-20) is used as the detector to capture the emitted SH signal. Figure 2(b) shows the power relation between measured SH counts and the input laser power at pump wavelength of 1440 nm, where the fitting curve is quadratic–exponential to the power of 2.0. The result confirms that the collected signals are indeed from the second-order nonlinear process. Figure 2(c) shows the measured $\chi^{(2)}$ spectrum (black diamonds) in comparison with the theoretically calculated result (red curve) from Eq. (1). Details of the $\chi^{(2)}$ derivation from the SHG measurement are discussed in the Supplement 1. The experimentally measured resonant $\chi^{(2)}$ peak reaches 2840 pm/V at 1440 nm, which is in good accordance with that from the theory. The large $\chi^{(2)}$ achieved in this cMQWs designed for the telecom wavelength is about 2 times higher than that at 920 nm in our previous work [12,17] and 40 times higher than that of traditional nonlinear crystals such as $LiNbO_3$.

The third-order nonlinear process is observed by the optical Kerr effect. Based on the quantum electrostatic model for metallic QW in our previous work [14,18], the expression for the third-order susceptibility $\chi^{(3)}$ is

$$\chi^{(3)}_{kjih}(\omega_1+\omega_2+\omega_3;\omega_1,\omega_2,\omega_3)=\frac{N}{\varepsilon_0\hbar^3}P_I\sum_{nmpl}\{$$
$$\frac{[\rho^{(0)}_{mm}-\rho^{(0)}_{ll}]\mu^k_{mn}\mu^j_{np}\mu^i_{pl}\mu^h_{lm}}{[\omega_{nm}-\omega_1-\omega_2-\omega_3-i\gamma_{nm}][\omega_{pm}-\omega_1-\omega_2-i\gamma_{pm}][\omega_{lm}-\omega_1-i\gamma_{lm}]}$$
$$-\frac{[\rho^{(0)}_{ll}-\rho^{(0)}_{pp}]\mu^k_{mn}\mu^j_{np}\mu^i_{lm}\mu^h_{pl}}{[\omega_{nm}-\omega_1-\omega_2-\omega_3-i\gamma_{nm}][\omega_{pm}-\omega_1-\omega_2-i\gamma_{pm}][\omega_{pl}-\omega_1-i\gamma_{pl}]}$$
$$+\frac{[\rho^{(0)}_{ll}-\rho^{(0)}_{nn}]\mu^k_{mn}\mu^j_{pm}\mu^i_{lp}\mu^h_{nl}}{[\omega_{nm}-\omega_1-\omega_2-\omega_3-i\gamma_{nm}][\omega_{np}-\omega_1-\omega_2-i\gamma_{np}][\omega_{nl}-\omega_1-i\gamma_{nl}]}$$
$$-\frac{[\rho^{(0)}_{pp}-\rho^{(0)}_{ll}]\mu^k_{mn}\mu^j_{pm}\mu^i_{nl}\mu^h_{lp}}{[\omega_{nm}-\omega_1-\omega_2-\omega_3-i\gamma_{nm}][\omega_{np}-\omega_1-\omega_2-i\gamma_{np}][\omega_{lp}-\omega_1-i\gamma_{lp}]}\},\quad\textbf{(2)}$$

where N is the density of free electrons, $\rho^{(0)}_{ll}$ is the population of electrons in-state l, and μ_{mn} is the dipole transition element related to the transition between state m and n. The intrinsic permutation operator P_I considers all possible permutation. In the special case of the Kerr response, three different permutations need to be considered: (1) $\omega_1=\omega_2=\omega_0$, $\omega_3=-\omega_0$; (2) $\omega_1=\omega_3=\omega_0$, $\omega_2=-\omega_0$; and (3) $\omega_2=\omega_3=\omega_0$, $\omega_1=-\omega_0$. A detailed derivation of the equation is explained in the Supplement 1.

In addition, the nonlinear refractive index n_2, also known as the Kerr coefficient, can be derived from the relation:

$$Re\{n_2\}=283\frac{Im\{\chi^{(3)}\}\times k_0+Re\{\chi^{(3)}\}\times n_0}{n_0({n_0}^2+{k_0}^2)},\quad\textbf{(3-1)}$$

$$Im\{n_2\}=283\frac{Im\{\chi^{(3)}\}\times n_0-Re\{\chi^{(3)}\}\times k_0}{n_0({n_0}^2+{k_0}^2)}.\quad\textbf{(3-2)}$$

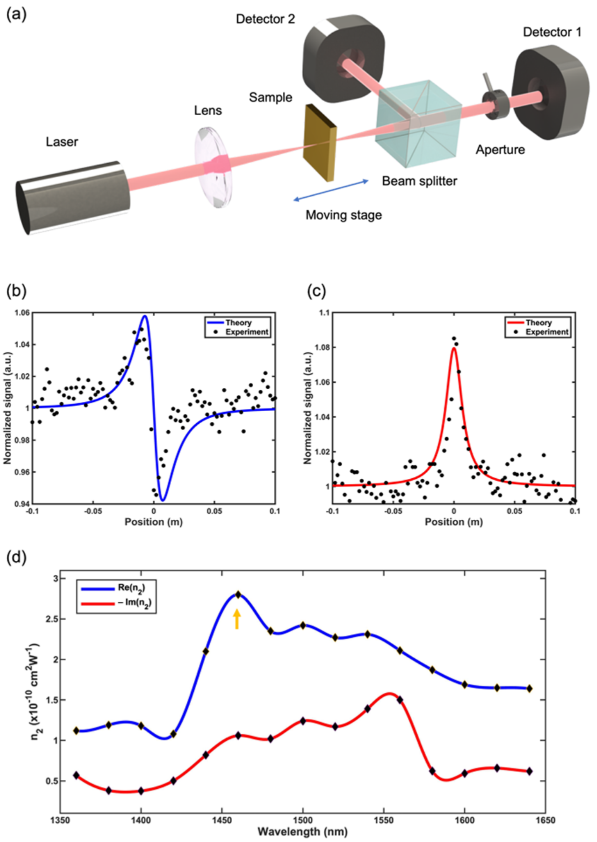

Fig. 3. (a) Optical setup of z-scan measurement for n_2 characterization. Recorded (b) closed aperture and (c) open aperture signals. (d) Derived wavelength dependent real and imaginary parts of the complex Kerr coefficient n_2 with spline fitting. The orange arrow points at the peak aligned to the corresponding ISBT wavelength shown in Fig. 1.

As drawn in Fig. 3(a), a z-scan measurement is performed to characterize the large third-order nonlinearity of the cMQW unit. The same laser system as the one used in the SHG measurement is applied. A lens is used to focus the p-polarized light at 45° angle of incidence onto the sample, which is placed on a motorized translation stage moving along the z axis direction of the lens. Next, the transmitted optical signal passing through an aperture then recorded by detector 1 (Thorlabs, PDA50B2) is identified as the closed aperture signal, while that by detector 2 (Thorlabs, PDA50B2) without an aperture is the open aperture signal. The recorded data at wavelength of 1460 nm are plotted and fitted in Figs. 3(b) and 3(c), respectively. Details of fitting parameters and equations are listed in the Supplement 1. By fitting the acquired data at different wavelengths, the spectral response of the third-order nonlinearity, namely the complex Kerr coefficient n_2, can be obtained. Figure 3(d) shows the real part and imaginary part of n_2 with spline fitting. The experimentally measured n_2 reaches $(2.8–1.1i)\times10^{-10}$ cm²/W at 1460 nm, where the orange arrow points at the peak resulting from the ISBTs between |1> & |2> and |2> & |3, as shown in Fig. 1(b). According to Eq. (3–1), the peak location of the real part of n_2 is mainly determined by the imaginary part of $\chi^{(3)}$, which is closer to the resonant transition. The large n_2 achieved in this cMQWs at the telecom wavelength is comparable to the findings in our previous work [14] and several orders higher than that of common materials such as Si or bulk Au.

In summary, we have demonstrated the theoretical and experimental realization of a material platform exhibiting unprecedentedly high optical second- and third-order nonlinearities at telecom wavelength. By leveraging the engineered electronic subbands in TiN-based cMQWs, we have crafted doubly resonant ISBTs for enhanced second-order nonlinearity and single-photon transitions for elevated third-order nonlinearity at the same time. The achievement of the second-order susceptibility $\chi^{(2)} = 900\text{–}2840\,\text{pm/V}$ and Kerr coefficient $n_2 = 1.1\text{–}2.8 \times 10^{-10}\,\text{cm}^2/\text{W}$ in 1400–1600 nm range highlights the outstanding potential of this material. Combining these two nonlinear optical properties within one material system provides a building block that offers more versatility and functionality for applications in nonlinear optics and photonics.

Funding. Defense Sciences Office, DARPA (HR00111820038); National Science Foundation (ECCS-2025752); U.S. Department of Energy (DE-SC0022134).

Acknowledgment. The authors acknowledge funding support from DARPA DSO-NLM Program (Grant No. HR00111820038). This work was performed in part at the San Diego Nanotechnology Infrastructure (SDNI) of UCSD, a member of the National Nanotechnology Coordinated Infrastructure, which is supported by the National Science Foundation (Grant No. ECCS-2025752). Work done by J. C. W. and W. X. was supported by the Department of Energy (Grant No. DE-SC0022134).

Disclosures. The authors declare no conflicts of interest.

Data availability. Data underlying the results presented in this paper are not publicly available at this time but may be obtained from the authors upon reasonable request.

Supplemental document. See Supplement 1 for supporting content.

REFERENCES

1. T. Schneider, *Nonlinear Optics in Telecommunications* (Springer, 2004).
2. P. J. Campagnola and L. M. Loew, Nat. Biotechnol. **21**, 1356 (2003).
3. Z. Zhang, C. Yuan, S. Shen, *et al.*, npj Quantum Inf. **7**, 123 (2021).
4. J. M. Dudley, G. Genty, and S. Coen, Rev. Mod. Phys. **78**, 1135 (2006).
5. P. Del'Haye, A. Schliesser, O. Arcizet, *et al.*, Nature **450**, 1214 (2007).
6. T. J. Kippenberg, R. Holzwarth, and S. A. Diddams, Science **332**, 555 (2011).
7. Z. Chai, X. Hu, F. Wang, *et al.*, Adv. Opt. Mater. **5**, 1600665 (2017).
8. T. Volz, A. Reinhard, M. Winger, *et al.*, Nat. Photonics **6**, 605 (2012).
9. M. Ono, M. Hata, M. Tsunekawa, *et al.*, Nat. Photonics **14**, 37 (2020).
10. J. Zhou, H. Qian, C.-F. Chen, *et al.*, Nano Lett. **21**, 330 (2021).
11. J. Zhou, J. Zhao, Q. Wu, *et al.*, Adv. Funct. Mater. **32**, 2204734 (2022).
12. H. Qian, S. Li, C.-F. Chen, *et al.*, Light: Sci. Appl. **8**, 13 (2019).
13. S. E. Bopp, H. Qian, S. Li, *et al.*, Appl. Phys. Lett. **116**, 241105 (2020).
14. H. Qian, S. Li, Y. Li, *et al.*, Sci. Adv. **6**, 3456 (2020).
15. H. Qian, Y. Xiao, and Z. Liu, Nat. Commun. **7**, 13153 (2016).
16. H. Qian, S. Li, S.-W. Hsu, *et al.*, Nat. Commun. **12**, 3111 (2021).
17. C.-F. Chen, H. Qian, and Z. Liu, Adv. Opt. Mater. **12**, 2302176 (2024).
18. S. Li, H. Qian, and Z. Liu, Adv. Funct. Mater. **30**, 2000829 (2020).